Chapter 6
Nonlinear Dynamics of Reactive Nanosystems: Theory and Experiments

Y. De Decker, D. Bullara, C. Barroo and T. Visart de Bocarmé

Reactive systems are known to give birth to complex spatiotemporal phenomena, when they are maintained far enough from their equilibrium state. There are literally hundreds of experimental evidences showing the emergence of such self-organized behaviors at the macroscopic scale. Examples include the appearance of regular oscillations of concentration in both space and time, the formation of stationary spatial organization of reactants and products, and the emergence of spatiotemporal chaos, to cite but a few examples.

The theoretical understanding of these phenomena can be considered as being well established. Chemical reactions play a central role in the appearance of complex behaviors because they are nonlinear processes. Indeed, the rates of reactions are typically polynomials of the concentrations and moreover include constants that depend exponentially on the temperature. Because of this, the equations ruling the spatiotemporal development of chemical reactions, which often take the form of reaction-diffusion equations, admit complicated (and even sometimes multiple) solutions. The number and the type of solutions change abruptly for some precise combinations of the parameters of the system, which are known as bifurcation points. This feature explains why new dynamical behaviors are observed only whenever a

Y. De Decker (✉) · D. Bullara · C. Barroo · T. Visart de Bocarmé
Center for Nonlinear Phenomena and Complex Systems,
Université Libre de Bruxelles (ULB),Campus Plaine C.P. 231.,
1050 Brussels, Belgium
e-mail: yannick.de.decker@ulb.ac.be

D. Bullara
e-mail: dbullara@ulb.ac.be

C. Barroo
e-mail: cbarroo@ulb.ac.be

T. Visart de Bocarmé
e-mail: tvisart@ulb.ac.be

S.C. Müller and J. Parisi (eds.), *Bottom-Up Self-Organization in Supramolecular Soft Matter*, Springer Series in Materials Science 217,
DOI 10.1007/978-3-319-19410-3_6

system is put far away from its equilibrium position, i.e. it must cross a bifurcation point before qualitatively different solutions can emerge.

While quite appealing, the above picture is incomplete, in the sense that it does not explain the molecular origin of complex phenomena. It is indeed based entirely on a macroscopic approach to physicochemical processes. One could wonder how, say, oscillations "get born" at the microscopic level and subsequently invade the whole system to give macroscopically observable changes. Such mechanisms are in fact implicitly included in the traditional reaction-diffusion approach, for which the emergence of new dynamical behaviors implies the existence of spontaneous fluctuations of the composition or of the other variables. The question of the emergence of complex dynamics should be answered, in principle, by relying on a fully microscopic description based on the classical or quantum equations of motion. The complexity of such an approach however makes it practically impossible to assess the collective behavior of reactive systems. To answer the above questions, a middle road has thus been proposed.

This intermediate, mesoscopic level of description is known as the *stochastic* approach to reactive systems. The basic idea is to consider chemical events as random processes that create or destroy a finite amount of particles. In this way, the discrete molecular character of a system's chemical composition is included in a natural way, and reflects itself in the form of fluctuations. The properties of these stochastic processes are not arbitrary but must respect well-defined constraints ensuring that they indeed describe correctly the chemistry and the physics of the system under consideration.

The most fruitful and popular stochastic approach is based on what is known as the *chemical master equation*, which is an evolution equation for the probability to find the system in a given chemical state at a given time. This approach relies on the hypothesis that reactive processes are Markovian, in other words that a system's chemical state at a given moment solely depends on the state it was in a very short time before. We will present this equation, as well as its most prominent properties, in Sect. 6.1. A special emphasis will be put on the properties of systems of a moderately small size. In such cases, the role and the properties of fluctuations can be evaluated more simply and in a more generic fashion. We introduce to this end a simplification of the chemical master equation: the chemical Fokker-Planck equation.

As mentioned before, the chemical master equation represents a powerful approach from which many theoretical conclusions can be drawn on the behavior of nonlinear reactions at small scales. Extremely exciting predictions can be made, for example, concerning the very possibility of having regular chemical oscillations at the nanometric level. While most of these predictions were supported by molecular dynamics simulations early on, the possibility to test them experimentally is much more recent. It is only recently indeed that techniques with a sufficient temporal and spatial resolution could be developed. Several advanced experimental techniques can be used to track the changes in the chemical composition of a surface. However, as of today only *field emission and field ion microscopy* have the capability of following chemical reactions in real time and real space, with a lateral resolution of a few Angströms. The

basics of these techniques, which characterize the surface composition of metallic samples shaped as nanometric tips, are given in Sect. 6.2.

Using both the stochastic theoretical approach and experimental results, we assess in the next sections the behavior of two important classes of systems. We first focus on the case of bistability (Sect. 6.3). Multistability is a very frequent instance of nonlinear response. For a given set of parameters, a reactive system can be found in one of several accessible time-invariant states. From a macroscopic point of view, the state that is selected depends on the history of the system, i.e. on the way it has been prepared. Stochastic theories predict that, because of fluctuations, a system can be "delocalized" between all these steady states, and that the time spent in each of these state is representative of its relative stability. We investigate whether this is true or not for a well-characterized reaction, namely for the oxidation of hydrogen on a catalytic substrate (rhodium).

We next turn to the important problem of oscillating reactions, in Sect. 6.4. The robustness of oscillations in the presence of fluctuations is a question of interest not only for the basic study of nanometric systems, but also for the understanding of living systems, for which regular oscillations have been observed at the level of a single cell. We here consider again a system consisting of a non-equilibrium chemical reaction, the reduction of NO_2 by H_2, taking place on a metallic tip (platinum, in this case). We show that the observed oscillations respect the predictions based on the chemical Fokker-Planck equation. Moreover, we demonstrate that despite the intrinsic noise, the system presents a low-dimensional dynamical attractor, just like the macroscopic oscillators do.

We conclude (Sect. 6.5) by a discussion on the implications these observations could have on the properties of self-organization for nanostructured materials.

6.1 The Chemical Master Equation

The emergence of complex, collective behaviors of reactive molecules should ideally be deduced from the use of first principles at a microscopic level. As of today, and despite recent impressive advances, it is still impossible to analyze or simulate the behavior of several hundreds or thousands of molecules described by Newton's or Schrödinger's law, for long enough times. Indeed, the typically nonlinear dynamics that characterizes non-equilibrium reactions takes place on time scales that are much larger than the inverse of the collision frequency.

A powerful alternative has been proposed to circumvent this problem. Instead of describing all the microscopic degrees of freedom, one can consider mesoscopic variables, such as the number of particles of each species. The idea is to consider that these numbers define stochastic processes, in the sense that they can be seen as sequences of random values over time. In this view, one can associate a joint probability to each of the possible histories of a system, i.e. to each of the possible successions of values that the stochastic variables can take. Define the number of

particles at time t as $\mathbf{n}_t = \{n_i(t)\}$, where i stands for each of the c constituents of the system. Then, the probability of a given path ω reads

$$P(\omega) = P(\mathbf{n}_{t_1}, t_1\,;\, \mathbf{n}_{t_2}, t_2\,;\, \ldots \mathbf{n}_{t_k}, t_k) \tag{6.1}$$

with $t_1 \geq t_2 \cdots \geq t_k$. It is also relevant to define the conditional probability

$$\begin{aligned} P(\omega|\alpha) &= P(\mathbf{n}_{t_1}, t_1\,;\, \mathbf{n}_{t_2}, t_2\,;\, \ldots \mathbf{n}_{t_k}, t_k|\mathbf{n}_{\tau_1}, \tau_1\,;\, \mathbf{n}_{\tau_2}, \tau_2\,;\, \cdots \mathbf{n}_{\tau_j}, \tau_j) \\ &\equiv \frac{P(\mathbf{n}_{t_1}, t_1\,;\, \mathbf{n}_{t_2}, t_2\,;\, \ldots \mathbf{n}_{t_k}, t_k; \mathbf{n}_{\tau_1}, \tau_1\,;\, \mathbf{n}_{\tau_2}, \tau_2\,;\, \ldots \mathbf{n}_{\tau_j}, \tau_j)}{P(\mathbf{n}_{\tau_1}, \tau_1\,;\, \mathbf{n}_{\tau_2}, \tau_2\,;\, \ldots \mathbf{n}_{\tau_j}, \tau_j)}, \end{aligned} \tag{6.2}$$

in which $t_1 \geq t_2 \geq \cdots t_k \geq \tau_1 \geq \tau_2 \geq \cdots \tau_j$. This quantity represents the probability to have the path ω, given that the system has been through a path α.

A simple balance equation can be obtained for probabilities, under the *Markovian assumption*. A Markov process is a process in which the future of a system can be deduced from its present state only. This property leads to a simplification of the path probabilities. It means that the probability to observe three successive values $\mathbf{n}_{t_1}$, $\mathbf{n}_{t_2}$ and $\mathbf{n}_{t_3}$ is given by

$$\begin{aligned} P(\mathbf{n}_{t_1}, t_1\,;\, \mathbf{n}_{t_2}, t_2\,;\, \mathbf{n}_{t_3}, t_3) &= P(\mathbf{n}_{t_1}, t_1|\mathbf{n}_{t_2}, t_2\,;\, \mathbf{n}_{t_3}, t_3)\, P(\mathbf{n}_{t_2}, t_2\,;\, \mathbf{n}_{t_3}, t_3) \\ &= P(\mathbf{n}_{t_1}, t_1|\mathbf{n}_{t_2}, t_2)\, P(\mathbf{n}_{t_2}, t_2\,;\, \mathbf{n}_{t_3}, t_3). \end{aligned} \tag{6.3}$$

Summing over all the possible intermediate states $\mathbf{n}_{t_2}$ between $\mathbf{n}_{t_3}$ and $\mathbf{n}_{t_1}$, one obtains the Chapman-Kolmogorov equation,

$$P(\mathbf{n}_{t_1}, t_1\,;\, \mathbf{n}_{t_3}, t_3) = \sum_{\mathbf{n}_{t_2}} P(\mathbf{n}_{t_1}, t_1|\mathbf{n}_{t_2}, t_2)\, P(\mathbf{n}_{t_2}, t_2; \mathbf{n}_{t_3}, t_3). \tag{6.4}$$

We will be interested here in the continuous-time limit of this equation. We introduce for this $\Delta t = t_1 - t_2 \ll 1$ and $t = t_2$ and define the transition probabilities per unit time,

$$W(\mathbf{n}|\mathbf{n}') \equiv \lim_{\Delta t \to 0} \left[\frac{P(\mathbf{n}_{t_1}, t_1|\mathbf{n}_{t_2}, t_2)}{\Delta t} \right] \geq 0,$$

in which we used the simplified notations $\mathbf{n} = \mathbf{n}_{t_1}$ and $\mathbf{n}' = \mathbf{n}_{t_2}$. By performing the Taylor expansion

$$\begin{aligned} P(\mathbf{n}_{t_1}, t_1\,;\, \mathbf{n}_{t_3}, t_3) &= P(\mathbf{n}, t + \Delta t\,;\, \mathbf{n}_{t_3}, t_3) \\ &\approx P(\mathbf{n}, t\,;\, \mathbf{n}_{t_3}, t_3) + \Delta t \, \frac{d}{dt} P(\mathbf{n}, t\,;\, \mathbf{n}_{t_3}, t_3) \end{aligned} \tag{6.5}$$

and a summation over the states $\mathbf{n}_{t_3}$ in (6.4), one finally arrives to the time-continuous master equation

$$\frac{d}{dt}P(\mathbf{n},t) = \sum_{\mathbf{n}'\neq\mathbf{n}} \left[W(\mathbf{n}|\mathbf{n}')P(\mathbf{n}',t) - W(\mathbf{n}'|\mathbf{n})P(\mathbf{n},t)\right].$$

Note that in order to obtain this result, we used the important property $\sum_{\mathbf{n}'} W(\mathbf{n}'|\mathbf{n}) = 0$.

This equation is an evolution law for the probability to find the system in a given state, at a given time. It is a valid representation of the fluctuating dynamics of a system, as long as the Markovian assumption holds. This hypothesis has been shown to hold for most reactive systems: It is expected to fail only in the case of rarefied gases, or for extremely fast reactions. The transition probabilities reflect the fact that a system can switch from one configuration to another. For reactive systems, these transitions are induced by the reactions themselves. It is thus convenient to formulate the above equation in terms of the r possible chemical processes. One can associate to each elementary event $\rho = 1, 2, \ldots r$ a stoichiometric equation

$$\sum_{i=1}^{c} \nu_{\rho,i}^{+} X_i \rightarrow \sum_{i=1}^{c} \nu_{\rho,i}^{-} X_i.$$

In this equation, X_i represents one of the species, the $\nu_{\rho,i}^{+}$s are the molecularities of the reactants, and the $\nu_{\rho,i}^{-}$s the molecularities of the products. Each elementary reaction thus induces a change $\nu_{\rho,i} = \nu_{\rho,i}^{-} - \nu_{\rho,i}^{+}$ in the number of particles of species i, defining the vector $\boldsymbol{\nu}_\rho = \left\{\nu_{\rho,i}\right\}$. The state $\mathbf{n} + \boldsymbol{\nu}_\rho$ reached after each reaction ρ is solely determined by the initial state $\mathbf{n}$ and by the nature of the reaction. We will therefore adopt the more convenient notation $W(\mathbf{n}+\boldsymbol{\nu}_\rho|\mathbf{n}) \equiv W_\rho(\mathbf{n})$, where $W_\rho(\mathbf{n})$ is known as the propensity function. Consequently, the master equation can be rewritten as

$$\frac{d}{dt}P(\mathbf{n},t) = \sum_{\rho=1}^{r} \left[W_\rho(\mathbf{n}-\boldsymbol{\nu}_\rho)P(\mathbf{n}-\boldsymbol{\nu}_\rho,t) - W_\rho(\mathbf{n})P(\mathbf{n},t)\right], \tag{6.6}$$

an equation known as the *chemical master equation*.

In principle, the above equation can be solved or used to derive evolution equations for the different moments of the underlying probability distribution, such as the mean or the variance of the concentrations. However, it can be solved exactly only for a few simple cases, and one typically has to resort either to approximations, or to numerical investigations. The most instructive analytical, albeit approximate results are obtained in the limit of moderately small systems, also called the weak-noise limit.

6.1.1 The Chemical Fokker-Plank Equation

The chemical master equation provides an exact representation of a reactive system inasmuch as the Markovian hypothesis holds. Its discrete character appears to be a natural choice for chemical systems, because a reaction always involves a finite number of molecules. However, dealing with discrete variables and equations is typically more difficult than working in a continuous framework.

For this reason, a first approximation which leads to a simpler yet analytical form of the master equation is to assume that the number of molecules of each species can change in a continuous fashion. This approximation holds as long as these number are much larger than 1 or, in other words, if the system is not too small. Having continuous variables allows one to expand the term $f_\rho(\mathbf{n}-\boldsymbol{\nu}_\rho) \equiv W_\rho(\mathbf{n}-\boldsymbol{\nu}_\rho)P(\mathbf{n}-\boldsymbol{\nu}_\rho, t)$ in (6.6) in Taylor series as

$$f_\rho(\mathbf{n}-\boldsymbol{\nu}_\rho) = f_\rho(\mathbf{n}) - \sum_{i=1}^{s} \nu_{\rho,i} \frac{\partial f_\rho(\mathbf{n})}{\partial n_i} + \frac{1}{2} \sum_{i,j=1}^{s} \nu_{\rho,i}\nu_{\rho,j} \frac{\partial^2 f_\rho(\mathbf{n})}{\partial n_i \partial n_i} + \cdots . \quad (6.7)$$

Substituting the above expansion in the chemical master equation allows one to express the time derivative of the probability as a series known as the Kramers-Moyal expansion. The main advantage of the Kramers-Moyal approach is that it leads to an expression of the master equation in terms of probabilities and propensity functions evaluated around a single reference state. However, the resulting equation is an a priori infinite sum, which still represents an intractable problem.

In order to obtain a more useful equation, the Kramers-Moyal expansion needs to be truncated to some order of a physically meaningful parameter. As suggested by van Kampen [1], it needs to be a parameter that naturally enters the transition probabilities, and at the same time governs the amplitude of the fluctuations. The most natural choice is to consider a parameter Ω of the system which is a measure of its size (such as the volume or the total number of particles). One can then introduce the intensive quantities

$$\mathbf{x} \equiv \{x_i\} \equiv \left\{\frac{n_i}{\Omega}\right\} \equiv \frac{\mathbf{n}}{\Omega}. \quad (6.8)$$

and re-expressing the probabilities in terms of these new variables

$$\mathcal{P}(\mathbf{x}, t) \equiv \Omega^s P(\Omega\mathbf{x}, t), \quad (6.9)$$

in which s is the total number of variables. Using (6.8), (6.9) and the above Taylor expansion in (6.6), we obtain

$$\frac{d}{dt}\mathcal{P}(\mathbf{x},t) = \sum_{m=1}^{\infty} \frac{(-1)^m}{m!\,\Omega^{m-1}} \sum_{i,j,\cdots,k=1}^{s} \frac{\partial^m}{\partial x_i \partial x_j \cdots \partial x_k} \times \left\{ \left[\frac{1}{\Omega} \sum_{\rho=1}^{r} \nu_{\rho,i}\nu_{\rho,j}\cdots\nu_{\rho,k} W_\rho(\Omega\mathbf{x}) \right] \mathcal{P}(\mathbf{x},t) \right\}. \quad (6.10)$$

For monomolecular, bimolecular and trimolecular reactions, it is found that for sufficiently large numbers of molecules the transition probability $W_\rho(\Omega\mathbf{x})$ can be approximately expressed as a linear function of the extensive parameter Ω [2], so that the terms in square brackets in (6.10) are practically independent from Ω.

For infinitely large systems, only the term corresponding to $m = 1$ survives in (6.10). This situation describes a system where the random fluctuations are completely ignored or, in other words, a deterministic system. For moderately small systems the sum can be truncated to its dominant contributions in Ω^{-1}. This situation is known as the *weak-noise limit*, and the resulting equation is called the *chemical Fokker-Planck equation*:

$$\frac{d}{dt}\mathcal{P}(\mathbf{x},t) = -\sum_{i=1}^{s} \frac{\partial}{\partial x_i}\left[F_i(\mathbf{x})\mathcal{P}(\mathbf{x},t)\right] + \frac{1}{\Omega}\sum_{i,j=1}^{s} \frac{\partial^2}{\partial x_i \partial x_j}\left[Q_{i,j}(\mathbf{x})\mathcal{P}(\mathbf{x},t)\right], \quad (6.11)$$

with

$$F_i \equiv \frac{1}{\Omega}\sum_{\rho=1}^{r} \nu_{\rho,i}\, W_\rho(\Omega\mathbf{x})$$

and

$$Q_{i,j} \equiv \frac{1}{2\,\Omega}\sum_{\rho=1}^{r} \nu_{\rho,i}\nu_{\rho,j}\, W_\rho(\Omega\mathbf{x}).$$

The first term of this equation acts as a "drift": The macroscopic evolution equation F_i steers the distribution along a well-defined path. The second term induces a "diffusion" of the probability distribution about that path, which captures the fact that fluctuations act as a noise that tends to broaden the distribution of concentrations.

This equation can be studied analytically to some extent and reveals especially fruitful in establishing general trends on the role played by fluctuations. Indeed, the Fokker-Planck equation admits solutions of the form [3, 4]

$$\mathcal{P}(\mathbf{x},t) = \exp\left[-\Omega\,\phi_0(\mathbf{x},t) - \phi_1(\mathbf{x},t) - \frac{\phi_2(\mathbf{x},t)}{\Omega} - \frac{\phi_3(\mathbf{x},t)}{\Omega^2}\cdots\right]. \quad (6.12)$$

By substituting (6.12) into (6.11), one obtains a hierarchy of coupled equations in powers of Ω. The equation at the leading order can be written under the form of a

Hamilton-Jacobi equation [5]

$$\frac{\partial \phi_0}{\partial t} + H(\mathbf{x}, \mathbf{p}) = 0, \tag{6.13}$$

where the special Hamiltonian [6, 7]

$$H(\mathbf{x}, \mathbf{p}) = \sum_{i,j=1}^{s} Q_{i,j}(\mathbf{x}) p_j p_k + \sum_{j=1}^{s} F_j(\mathbf{x}) p_j$$

depends on the generalized momenta

$$\mathbf{p} \equiv \frac{\partial \phi_0}{\partial \mathbf{x}} \equiv \left\{ \frac{\partial \phi_0}{\partial x_i} \right\} \equiv \{p_i\}.$$

If one limits oneself to the leading order in (6.12), an explicit formula for ϕ_0 is enough to calculate $\mathcal{P}(\mathbf{x}, t)$. The general solution for the Hamilton-Jacobi equation (6.13) is given by the action

$$\phi_0(\mathbf{x}, t) = \int (\mathbf{p} \cdot \mathrm{d}\mathbf{x} - H(\mathbf{x}, \mathbf{p})\, \mathrm{d}t), \tag{6.14}$$

with the integral being calculated over the trajectories of Hamilton's equations:

$$\dot{x}_i = \frac{\partial H}{\partial p_i} = F_i(\mathbf{x}) + 2 \sum_{j=1}^{s} Q_{i,j}(\mathbf{x})\, p_j, \tag{6.15}$$

$$\dot{p}_i = -\frac{\partial H}{\partial x_i} = -\sum_{j=1}^{s} \frac{\partial F_i(\mathbf{x})}{\partial x_i} p_j - \sum_{j,k=1}^{s} \frac{\partial Q_{j,k}(\mathbf{x})}{\partial x_i} p_j\, p_k. \tag{6.16}$$

Notice that the (6.15) is an evolution equation for the intensive variables, which contains the factors $F_i(\mathbf{x})$ and $Q_{j,k}(\mathbf{x})$, responsible for the "drift" and "diffusive" parts of the Fokker-Planck equation. More specifically for $\mathbf{p} = \mathbf{0}$, (6.15) reduces to the classical mean-field dynamics.

These expressions can be used to obtain approximate, but analytical and generic properties of the solutions to the Fokker-Planck equation. Before we do so, we will however present the experimental techniques that we used to assess the fluctuating behavior of chemical reactions at the nanoscale and, eventually, the validity of the above stochastic description.

6.2 Field Emission and Field Ion Microscopy

We present rapidly the two techniques that were used for the experimental results presented in the following sections, namely field emission and field ion microscopy. The field ion microscope (FIM) is an evolution of the field electron emission microscope (FEM) developed earlier by the same inventor, Erwin W. Müller. The FIM permitted single atoms to be imaged for the first time in 1955 [8]. The context of the developments leading to the first pictures with atomic lateral resolution has been evoked by Melmed [9]. The field electron and the field ion microscopes are elegant in their simplicity of design and operation. An exhaustive review of the developments of these methods can be found in the textbook by Miller et al. [10].

A FEM consists in an evacuated glass or stainless steel vessel in which a sharp needle tip is pointing towards a phosphorescent screen. A difference of potential is applied between the tip and a counter-electrode, with the needle being negatively biased. A scheme of the device is presented in Fig. 6.1a. The voltage on the tip conjugated with the curvature of the apex causes the emission of electrons (if the electric field is of the order of $1\,\mathrm{V\ nm^{-1}}$). These electrons are accelerated by the electric field and their kinetic energy is converted to a light signal on the screen. The resulting picture illustrates the variations of the local work functions along a curved surface and corresponds to a magnified image of the surface at the level of the apex. An example is provided in Fig. 6.1c.

The local work function depends on the nature of the metal and on the crystallographic orientation of the plane from which the electrons are being extracted. It can also be modified by the presence of adsorbates. The local brightness varies accordingly and is monitored to follow dynamic changes occurring on the surface of the sample upon exposure to reactive gases or gas mixtures. The lateral resolution is of the order of 20 Å. The magnification is of 10^5 to 10^6 times and proportional to the D/R_c ratio, where D and R_c are the tip to screen distance and the radius of curvature of the apex, respectively. For ideal cases of monocrystalline samples, the symmetry of the patterns is sufficient to assign the Miller indices of most typical orientations of the crystal.

The evolution from FEM to FIM devices, leading to atomic lateral resolution, came with the introduction of a gas: the imaging gas. FIM imaging is achieved in the same device and with the same experimental set-up as for FEM (Fig. 6.1a), with the notable exception that in the FIM mode, the needle is biased positively. The specimen is cooled to cryogenic temperatures and a low amount of imaging gas, typically helium or neon at 10^{-5} mbar, is introduced into the system.

As the voltage on the specimen is increased, the atoms of the imaging gas that come close to the tip are polarized and attracted to the specimen by the inhomogeneous electric field (Fig. 6.1b). When the voltage on the specimen is increased to generate a sufficiently high field, typically $30–50\,\mathrm{V\ nm^{-1}}$, the atoms of the imaging gas on the surface are field ionized: A valence electron of the gas atom (or molecule) tunnels through the barrier of potential energy between the gas species and the surface. The resulting cations are projected towards the screen. The image of the surface

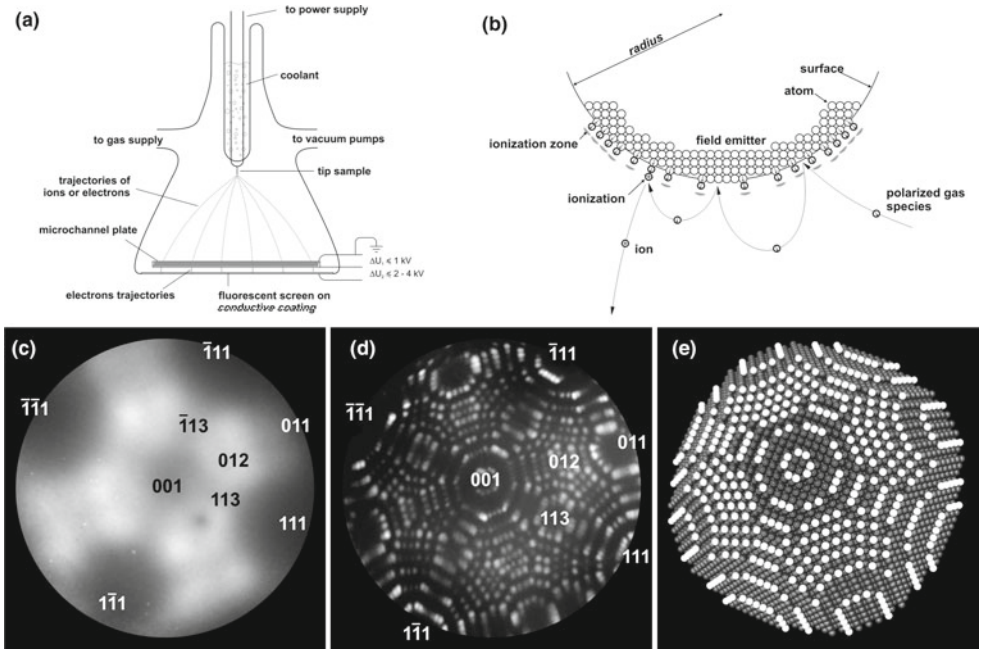

Fig. 6.1 **a** Scheme of a field ion microscope. **b** Ionization scheme of a polarized gas atom at the vicinity of the tip apex. **c** Field electron emission microscopy of a face-centered cubic metal. **d** Field ion microscopy of the same sample. **e** Ball model build according to the same crystal lattice given the shape of a quasi-hemisphere. Each ball depicts one single atom, with the *white* ones standing for the most protruding surface atoms

formed in this way is thus a mapping of the field ionization rate of the imaging gas over individual atoms at the surface of the entire apex region. Microchannel plate image intensifiers are positioned in front of the phosphorescent screen to increase the brightness on the screen by a factor of approximately 10,000. The final spatial resolution of the image is typically of 2 Å and allows single atoms to be imaged. A field ion image is shown in Fig. 6.1d alongside a ball model that serves as a guide to the eye (Fig. 6.1e). Note that when further increasing the intensity of the electric field, the surface atoms themselves can be field ionized and evaporated from the specimen as charged species. This process is termed field evaporation and reveals useful to clean the tip sample and also permits the bulk of the specimen to be examined.

The platinum and rhodium tips presented here are produced by electrochemical etching in a molten salt mixture of NaCl and $NaNO_3$ (1:4 w/w). The samples are initially characterized by FIM to assess the symmetry and the quality of the etching procedure. Cycles of thermal annealing, Ne^+ ion sputtering and field evaporation are used to clean the tips. The tip holders are built to allow the samples to be heated resistively. The temperature can be accurately measured by a Ni/NiCr thermocouple at the basis of the tip and controlled between 50 and ≈1,000 K with an accuracy of 0.1 K. Assuming a hemispherical shape, net plane counting between known orientations on the field ion micrograph provides an estimation of the radius of curvature.

Both FIM and FEM can be used to monitor chemical reactions in real time, at the nanoscale. In the remainder of this work, we will provide examples of nonlinear behaviors observed in this way. We start with an instance of bistability, as observed during the formation of water on rhodium.

6.3 Bistability in the $H_2 + O_2$/Rh System

The effects of fluctuations are predominantly felt in the case of nonlinear dynamics. As a first illustration, we consider the case of a bistable system at the nanoscale. Multistability consists in the coexistence of different steady states for a given choice of control parameters. It is very often encountered in systems presenting kinetic feedbacks, such as the heterogeneous catalytic systems we are analyzing here. In the macroscopic limit, the theory of dynamical systems predicts that one should observe for long enough times only one of the accessible stable steady states of the system. The state that will be selected depends on the initial conditions.

In the case of noisy systems, the spontaneous fluctuations of composition can induce transitions between the stable steady states. The unstable states that separate them act as activation barriers in this view. Consequently, for long enough times the state of the system is "delocalized" between the accessible states. This property reflects itself in the solutions of the Fokker-Planck equation. Remember that, for large enough systems, the probability density is given by

$$\mathcal{P}(\mathbf{x}, t) \sim \exp\left[-\Omega\, \phi_0(\mathbf{x}, t)\right] \tag{6.17}$$

The dominant function ϕ_0 is often called the stochastic potential. Generally speaking, in the case of multistable systems, the stochastic potential will present several minima for values of $\mathbf{x}$ that typically are close to the steady states of the macroscopic solution. The probability distribution will consequently present several maxima for these values. Because of the exponential character of the connection between $\mathcal{P}$ and ϕ_0, however, only the states that have similar values of the potential will be observed in the macroscopic limit. This explains why only one state should be observed for large systems, since the probability to find a metastable state is exponentially smaller than the probability to find the most stable state of the system.

To test whether fluctuating dynamics generate multi-humped probability distributions, we monitored the brightness of the image during the interaction of a rhodium (Rh) tip with a mixture of gaseous hydrogen and oxygen in the FIM mode. A freshly developed specimen is heated to a fixed temperature ranging between 400 and 550 K. A chosen gas mixture is introduced in the chamber at pressures ranging from 10^{-6} to 10^{-4} mbar, and a difference of potential is applied so as to develop a visible field ion pattern. Under reactive conditions, the temperature and the somewhat lower imaging fields (about 10 V nm^{-1}) do not allow for an atomic lateral resolution. However, it has been proven [11] by means of a direct local chemical analysis using a dedicated atom probe instrument [12] that an oxidized Rh surface appears "granular" and dark in FIM images. Brightness analysis can thus be used as a tool to qualitatively monitor whether the surface is locally in an oxidized or in a metallic state.

Figure 6.2 illustrates a series of field ion micrographs during a sequence where a Rh sample is put in contact with the reactive gases for a fixed pressure ratio p_{H_2}/p_{O_2}, at 450 K. For a fixed value of p_{O_2}, the p_{H_2}/p_{O_2} ratio can be varied from hydrogen rich (9:1) to hydrogen-poor environments. When decreasing the H_2 partial pressure while keeping the O_2 pressure constant, local transformations of the state of the surface are observed. Relatively bright regions turn into a darker, granular structure with relatively uniform brightness and without any indication of the symmetry of the underlying bulk material (see Fig. 6.2). The local chemical analysis of these regions shows the presence of Rh_xO_y species in the mass spectra, which confirms the presence of a surface oxide. At temperatures ranging from 400 to 500 K, surface oxides are particularly persistent on the zone lines located between the (001) topmost pole and the four {011} peripheral planes. These zones define a cross-like pattern that is discernible on the four panels of Fig. 6.2; they remain oxidized for most of the observations to be reported in this section. At high hydrogen pressures, most of the surface is in a metallic (bright) state. At low H_2 pressures, the whole surface appears to be in an oxidized state. For intermediate values, the system shows bistability with a hysteresis extending over a well-defined range of p_{H_2}/p_{O_2}. More precisely, the (001) oriented tip shows a fourfold symmetry, with four quadrants centered around a {111} pole. The bistability is made visible by FIM via abrupt and unpredictable modifications of the surface state of these quadrants flipping in an independent manner from the oxidized to the metallic states, and vice-versa. A kinetic phase diagram has been established earlier for this system [13, 14]. For high temperatures, i.e. close to 550 K, the bistability region shifts towards lower H_2 pressure and narrows considerably until it finally disappears.

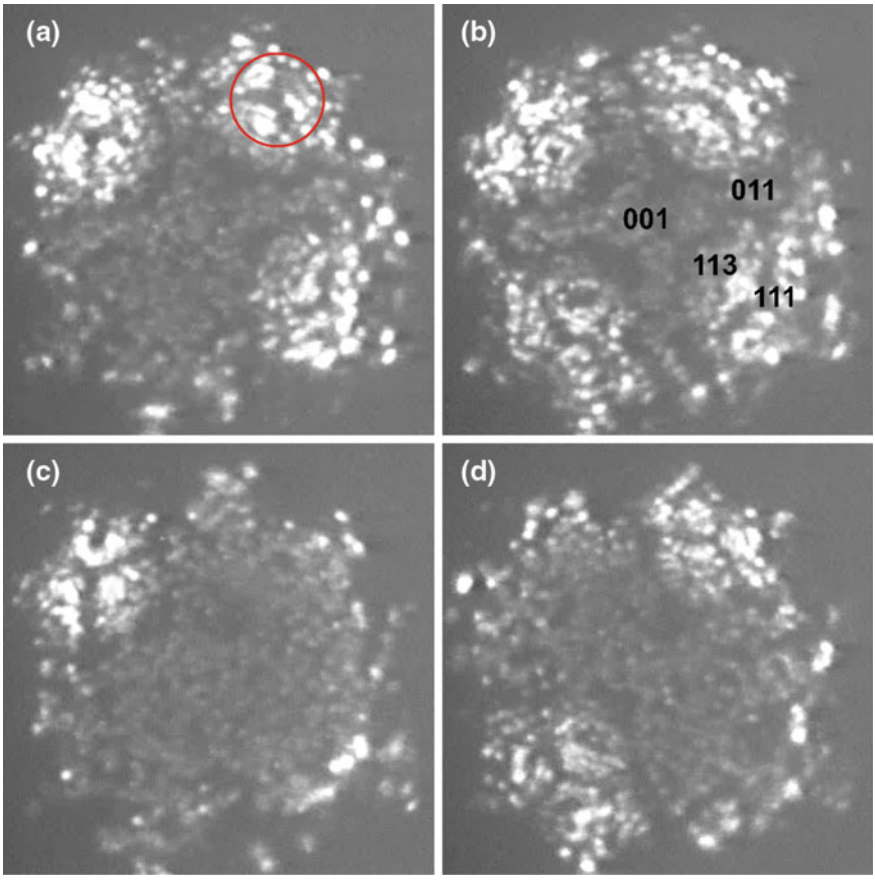

Fig. 6.2 Series of field ion micrographs acquired during the bistable regime of $O_2 + H_2$ reaction. On the four quadrants of the tip sample (as depicted on a), the system switches from an oxidized state to a metallic state. Conditions: $F = 10\,\mathrm{V\,nm^{-1}}$, $p_{O_2} = 5 \times 10^{-6}$ mbar, $p_{H_2} = 1.2 \times 10^{-5}$ mbar

Time series of the brightness monitored on each of the quadrants are presented in Fig. 6.3 for a temperature of 450 K. A comparison of Figs. 6.2 and 6.3 shows that a high intensity of the brightness is correlated with a metallic state of the surface. Conversely, a lower brightness is measured in the presence of a surface oxide. The four curves thus show local and erratic fluctuations of the surface between the oxidized and metallic states, with no noticeable correlation between the states of the quadrants. Consequently, the histograms counting the fraction of time spent in each of these states are bimodal in the region of bistability, in qualitative accordance with the stochastic predictions (see Fig. 6.4 corresponding to the last time series of Fig. 6.3). This feature persists for temperatures that allow the determination of a region of bistability. At $T \geq 550\,\mathrm{K}$, the reaction is less sensitive to the underlying structure

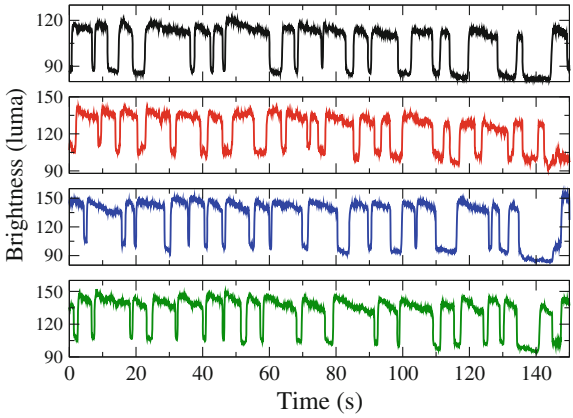

Fig. 6.3 Time series of the four quadrants extracted from the previous figure, showing transitions between an oxidized state (low brightness) and an oxygen-poor state (high brightness)

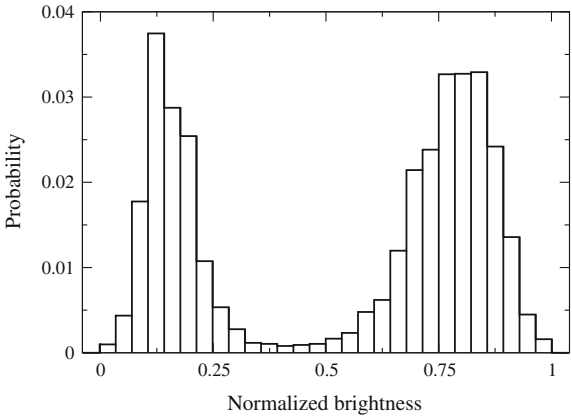

Fig. 6.4 Distribution of brightness for the time series presented on Fig. 6.3 (30 bins were used)

and the phenomenology turns to an oscillatory behavior that covers the entire visible surface area of the tip [15].

Although the probability is indeed bimodal as expected, one should make sure that it is indeed the chemistry of the reaction that is responsible for the bistability and the transition between the states. To show this, we consider here a "backbone" model for the reaction, which is a simplification of the complex, realistic model developed in [13, 14]. We first take into account the fact that oxygen adsorbs dissociatively on the surface:

$$O_2(g) + 2* \rightarrow 2\,O(ads), \tag{6.18}$$

an equation in which $*$ stands for an available active site on the surface of the metal. It should be noted that the oxygen adsorption has been shown to involve a precursor state. Moreover, the desorption of oxygen being very slow at the temperatures considered here, we neglect it for now. H_2 adsorbs as well in a dissociative way, and

its desorption is non-negligible under the conditions of the experiments, so that we consider the following steps

$$\mathrm{H_2(g)} + 2* \rightleftharpoons 2\,\mathrm{H(ads)}. \tag{6.19}$$

Once on the surface, hydrogen and oxygen adatoms combine to give water, which is known to readily desorb from Rh at such temperatures:

$$\mathrm{O(ads)} + 2\,\mathrm{H(ads)} \rightarrow 3\ * + \mathrm{H_2O(g)}. \tag{6.20}$$

Finally, we take into account the fact that oxygen adatoms can be removed from the quadrants either because they diffuse to the shanks of the tip, or because they go under the surface to form an oxide. We combine these two processes into an effective removal step

$$\mathrm{O(ads)} \rightarrow *. \tag{6.21}$$

These steps can be translated into transition probabilities per unit time quite straightforwardly under the hypotheses (i) that the system is well mixed, (ii) that the temperature is constant and (iii) that intermolecular interactions can be neglected. For the adsorption of oxygen, we use

$$W_1 = \frac{k_1\, K\, p_{\mathrm{O_2}}}{\Omega}\, \frac{(\Omega - N_\mathrm{O} - N_\mathrm{H})\,(\Omega - N_\mathrm{O} - N_\mathrm{H} - 1)}{1 + K\,\left(1 - \frac{N_\mathrm{O}}{\Omega} - \frac{N_\mathrm{H}}{\Omega}\right)^2} \tag{6.22}$$

In this equation, N_O and N_H stand for the number of adsorbed oxygen and hydrogen atoms, respectively. The value of Ω can be here assimilated to the total number of accessible active sites in each quadrant. The form of this adsorption term is specific of promoter-induced adsorption, as it includes an adsorption constant k_1, the equilibrium constant of the promoter/adsorbate transfer, K, and the pressure of oxygen. For hydrogen adsorption and desorption, there is no precursor state and we use simply

$$W_2 = \frac{k_2\, p_{\mathrm{H_2}}}{\Omega}\,(\Omega - N_\mathrm{O} - N_\mathrm{H})\,(\Omega - N_\mathrm{O} - N_\mathrm{H} - 1) \tag{6.23}$$

and

$$W_3 = \frac{k_3}{\Omega} N_\mathrm{H}\,(N_\mathrm{H} - 1). \tag{6.24}$$

Similarly, the reaction and the removal processes follow a simple mass-action type of law

$$W_4 = \frac{k_4}{\Omega^2}\, N_\mathrm{O}\, N_\mathrm{H}\,(N_\mathrm{H} - 1), \tag{6.25}$$

$$W_5 = k_5\, N_\mathrm{O} \tag{6.26}$$

Table 6.1 summarizes the numerical values of the parameters that were all calculated from the literature, except for the removal rate constant k_5 and the size Ω that act as a fitting parameters.

We assess the effect of fluctuations by simulating the different stochastic processes with Gillespie's algorithm [17]. In the macroscopic limit $\Omega \to \infty$, the model predicts the coexistence of an oxygen-poor and an oxygen-rich states, for a whole range of hydrogen pressures. For low enough values of the extensive parameter Ω, spontaneous transitions are observed between the two states. An example is depicted in Fig. 6.5, for the same values of the temperature and of the partial pressures as in the experiments. To make the comparison easier, we plotted the fraction of sites that are not occupied by oxygen, as a measure of the relative brightness of the surface (remember that an oxygen-rich surface appears darker). We observe that the transitions define a histogram whose shape is qualitatively comparable to what is measured experimentally. These results tend to prove that the chemical processes are the cause for the observed transitions. Note that a similar conclusion was reached earlier thanks to a FEM study of the CO + O_2 reaction on platinum [18]. The value of Ω we use was set so as to obtain a frequency of transitions that matches the exper-

Table 6.1 Values of the parameters used in the stochastic simulations of the H_2 + O_2 model

Parameter	Numerical value
k_1	2.73×10^5 mbar^{-1} s^{-1} [16]
k_2	1.09×10^6 mbar^{-1} s^{-1} [16]
k_3	2,084 s^{-1} [13]
k_4	10,214 s^{-1} [13]
k_5	0.45 s^{-1} [13]
K	24.72 [13]

The values taken from the literature were estimated at $T = 450$ K, neglecting the lateral interactions and the effects of the electric field

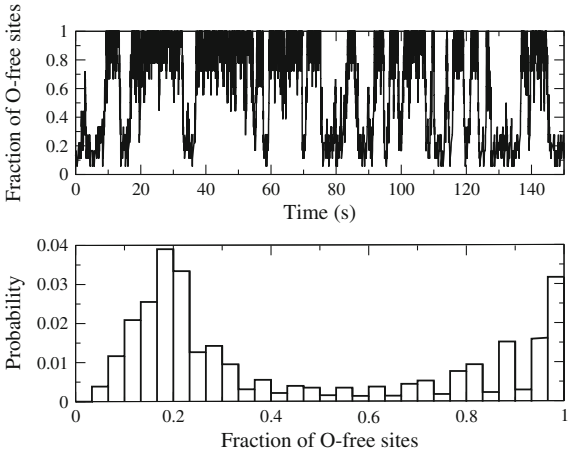

Fig. 6.5 Upper figure: outcome of a stochastic simulation, for $p_{O_2} = 5 \times 10^{-6}$ mbar, $p_{H_2} = 1.2 \times 10^{-5}$ mbar and $\Omega = 20$. The values of the other parameters are given in Table 6.1. Lower figure: histogram of the time spent in the oxygen-poor and oxygen rich states, to be compared with Fig. 6.4

imental observations, which leads to $\Omega \approx 20$. This number of sites is much lower than what is available over the entirety of each of the quadrants. This result indicates that the fluctuations leading to the transitions could involve only a limited number of particles on the surface, and that the fluctuation subsequently propagates to invade the whole quadrant. This hypothesis could be verified with the use of video systems with a better temporal resolution.

Multistability is not the only interesting nonlinear phenomenon that chemical reactions can induce. One of the most fascinating examples of complex reactive phenomena is the emergence of regular oscillations of concentrations, to which we now turn.

6.4 Oscillations During the $NO_2 + H_2$ Reaction on Platinum

This section reports on the observation of self-sustained periodic oscillations by means of FEM during the catalytic hydrogenation of NO_2 on Pt field emitter tips. The temperature of a freshly developed sample, similar to the one depicted on Fig. 6.1d, is first increased up to 390 K. A negative voltage is applied under UHV conditions, and is gradually increased so as to allow for the emission of electrons and to observe a clean field emission pattern. NO_2 is then injected in the chamber and dissociative adsorption occurs, leading to adsorbed oxygen species, which increases the work function on Pt [19] and consequently decreases the brightness. Hydrogen is then introduced in the system. For a constant base pressure of NO_2 (3.64×10^{-6} mbar in this particular case), the H_2 pressure is gradually increased, up to a maximum of 4×10^{-4} mbar (due to limitations of the technique).

Two distinct stable stationary states can be observed. The first one is characterized by a low level of brightness at low H_2 pressure, which has been assigned to a surface covered with O (ads) species. The second one, observed at large H_2 pressures only, is characterized by a relatively high level of brightness, which can be related to the surface being mostly covered with H(ads). In the intermediate range of pressure of hydrogen, nonlinear behaviors occur either in the form of aperiodic or periodic oscillations [20]. Aperiodic oscillations are observed whenever the control parameter is close to the transition from stationary state to oscillations, while periodic oscillations are seen far from this bifurcation point. All these nonlinear behaviors are characterized by transitions from a state of low brightness to a state of high brightness, and vice versa. All the active facets ignite simultaneously within the time resolution of the recording device (40 ms) [21]. The degree of activity of the reaction can be probed on any of the {012} facets (see Fig. 6.1d), because the change of brightness on these planes is high enough for imaging the process, and altogether low enough to avoid a saturation of the signal for a wide range of parameters. A comparison of the FEM and FIM patterns allows to estimate the size of the probed region as being $\approx 10\,\text{nm}^2$.

An example of the brightness signal during periodic oscillations is presented in Fig. 6.6a. During the experiments, all the control parameters (temperature, electric field and pressure of both gases) are kept constant: The observed behavior can be said

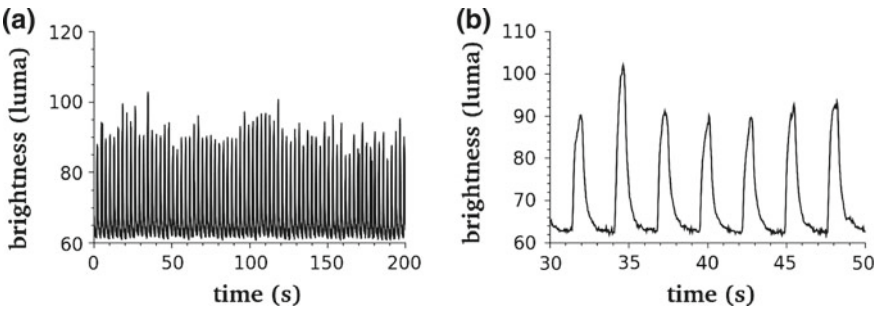

Fig. 6.6 **a** Brightness signal of self-sustained periodic oscillations. Conditions: $T = 390\,\mathrm{K}$, $F \approx 4\ \mathrm{V\ nm^{-1}}$, $p_{\mathrm{H_2}} = 1.46 \times 10^{-4}$ mbar, $p_{\mathrm{NO_2}} = 3.64 \times 10^{-6}$ mbar. **b** Magnification of a few cycles, highlighting the relaxation-type oscillation characterized by a sharp increase in brightness (fast relaxation) followed by a slower decrease of brightness (slow build-up)

to be self-sustained. The peaks first consist in a sharp increase of the brightness that has been assigned to the formation of water, which is known to decrease the work function [22]. The level of brightness then decreases with a slower pace, down to its initial value. This feature is typical of relaxation-type oscillations, for which all the "stress" accumulated during a slow build-up phase is released rapidly. The periodic character of the dynamics pictured in Fig. 6.6 is confirmed by Fourier power spectra of the time series, which show a well-defined period of $(2.72 \pm 0.06)\,\mathrm{s}$.

Because of the small size of the system, the spontaneous fluctuations of the chemical composition on the surface affect the properties of the oscillations. From a theoretical point of view, if the system were macroscopic the oscillations would be perfectly regular since they would be due to the fact that the dynamics defines a cycle in the phase space spanned by the concentrations of the different species. For moderately small systems, the effects of fluctuations can be assessed with the chemical Fokker-Planck equation introduced earlier. We focus more particularly on the Hamilton-Jacobi approach. In the absence of time-dependent forcing (which is the situation encountered in the experiments), the effective Hamiltonian is conserved since $dH/dt = 0$, which defines a constant pseudoenergy $E = H(\mathbf{x}, \mathbf{p})$. Under this condition, (6.14) relates the action $\phi_0(\mathbf{x}, t)$ to the reduced action $V(\mathbf{x}, E) = \int \mathbf{p} \cdot \mathrm{d}\mathbf{x}$, through the Legendre transform

$$\phi_0(\mathbf{x}, t) = V(\mathbf{x}, E) - E\,t. \tag{6.27}$$

Since $V(\mathbf{x}, E)$ is independent from t, the above Legendre transform implies that

$$\frac{\partial V}{\partial t} = \frac{\partial \phi_0}{\partial t} + E = 0 \quad \text{and} \quad \frac{\partial^2 \phi_0}{\partial t^2} = -\left(\frac{\partial t}{\partial E}\right)^{-1}. \tag{6.28}$$

An oscillating solution with period T hence describes a limit cycle in the subspace $\mathbf{p} = \mathbf{0}$, which implies $\mathbf{x}(t + rT) = \mathbf{x}(t)$ for $r = 0, \pm 1, \pm 2, \pm 1, \ldots$. Outside of this

subspace, for $\mathbf{p} \neq \mathbf{0}$, the limit cycle still exists but it is now deformed because of the effects of random fluctuations. It therefore has a different period $\mathcal{T}(E)$ which becomes equal to T as $E = 0$. If a trajectory starts from a point $\mathbf{x}_0$ located exactly on the macroscopic limit cycle with a phase θ_0, reaches a point $\mathbf{x}_*$ on the macroscopic limit cycle at a given phase θ_* after time $t_* = r\,T + \theta_* - \theta_0$, and finally ends in a close-by point $\mathbf{x}$ in the deformed limit cycle at time t, the action $\phi_0(\mathbf{x}, t)$ at the final position can be expressed as a Taylor series around its value at the intermediate position $\mathbf{x}_*$. Since the point $(\mathbf{x}_*, t_*)$ belongs to the macroscopic limit cycle, we can use (6.28) and the fact that $E = 0$ and $\mathbf{p} = \mathbf{0}$ to simplify the action as:

$$\phi_0(\mathbf{x}, t) = \frac{1}{2r\,|\partial T/\partial E|}(t - t_*)^2 + \frac{1}{2}\frac{\partial^2 \phi_0(\mathbf{x}_*, t_*)}{\partial \mathbf{x}^2} : (\mathbf{x} - \mathbf{x}_*)^2 + \cdots . \tag{6.29}$$

The general solution of the Fokker-Plank equation (6.12) thus reads

$$\mathcal{P}(\mathbf{x}, t|\mathbf{x}_0) \sim \exp\left[-\frac{\Omega}{2r\,|\partial T/\partial E|}(t - t_*)^2 - \frac{\Omega}{2}\frac{\partial^2 \phi_0(\mathbf{x}_*, t_*)}{\partial \mathbf{x}^2} : (\mathbf{x} - \mathbf{x}_*)^2\right], \tag{6.30}$$

which holds for $t_* - T/2 < t < t_* + T/2$. The probability distribution thus takes a Gaussian form around the macroscopic solution. The transverse extension of the distribution mostly depends on the stability properties of the limit cycle, while its longitudinal extension increases as $t \to \infty$ (because in this limit $r \simeq t/T$). The effect of a weak noise is to "diffuse" the phase of the oscillation along the limit cycle as time increases. Consequently, one can expect $\mathcal{P}(x, t)$ to define for long times a stochastic crater, whose ridge corresponds to the most probable shape of oscillation (i.e. to the limit cycle). Such stochastic craters have been observed in theoretical models, like the Brusselator. Combining several tools of nonlinear time series analysis, we now show that these stochastic objects can also be extracted from the system under consideration.

In the case of FEM experimental data, the brightness signal $B(t)$ is the only measurable variable. The first objective is to reconstruct, from this single measurement, the trajectories of the original phase space. We use to this end the classical tools of phase space reconstruction based on time delay embedding [23, 24]. In such an approach, a tentative phase space is constructed by plotting the original signal as a function of itself, but taken at a different time. The procedure can be repeated to generate an N-dimensional phase space. The two critical parameters that need to be determined are thus the optimal time delay and the dimensionality of the reconstructed space. The trajectories and the attractors constructed in such an optimally reconstructed space are known to be qualitatively similar to those of the real, inaccessible phase space.

In order to determine the dimensionality of the underlying phase space, we used the Average Mutual Information (AMI), which is a measure of the degree of correlation between measurements taken at different times. The AMI between points separated by a given delay is calculated, and the optimal value is chosen to correspond to the

first minimum of the AMI. For the time series presented here, we found an optimal time delay of 600 ms. The embedding dimension is another important quantity that needs to be computed. It represents the dimensionality of the space in which the attractor can be fully embedded. We rely here on the False Nearest Neighbors (FNN) method, which is known to be one of the most reliable approaches for noisy systems. The basic idea behind the FNN method is to find data points that are close in a space of dimension N, and to check if they remain so in a space of dimension $N + 1$. If they do not, the points were "false neighbors": The attractor constructed in the space of dimension N was a projection of a higher-dimensional object. The procedure is repeated until a convergence of the fraction of false neighbors is reached. Ideally, the proportion of FNNs should drop to 0 for the optimal embedding dimension. However, as we can see in Fig. 6.7, the percentage of FNNs drops to a minimum of 44.65. The subsistence of FNNs for high dimensions is a known consequence of the presence of fluctuations. In the present case, we observe that the percentage of false neighbors drops to 46.8 already for an embedding dimension of 2, and that it fluctuates around that value when the dimension is increased. We will consequently use a two-dimensional phase space.

The reconstructed phase space we use is thus spanned by $B(t)$ versus $B(t + 600\text{ms})$. We observe that the trajectories of the system presents closed loops, representative of a limit cycle. The fact that the oscillations can be captured in a low-dimensional space is a strong sign in favor of the existence of an underlying, almost deterministic dynamics. Going one step further in the analysis, we construct now 3D histograms from the data. We first coarse grain the phase space into boxes, the size of which is determined with Scott's rule. We subsequently calculate the the number of $(B(t), B(t+\tau))$ couples in each box and divide this by the total number of points. The quantity obtained in such a way is the relative probability that the system be in the corresponding "box" defined around each position in the reconstructed phase space. Plotting these probabilities as a function of the coordinates, the 2-dimensional

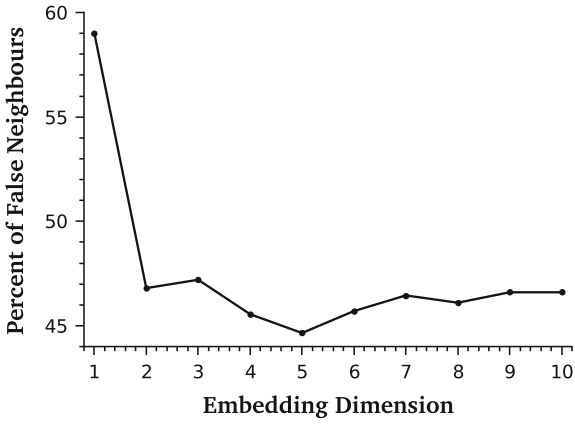

Fig. 6.7 Estimation of the embedding dimension by the False Nearest Neighbours method, as computed with the Visual Recurrence Analysis software (by Eugene Kononov)

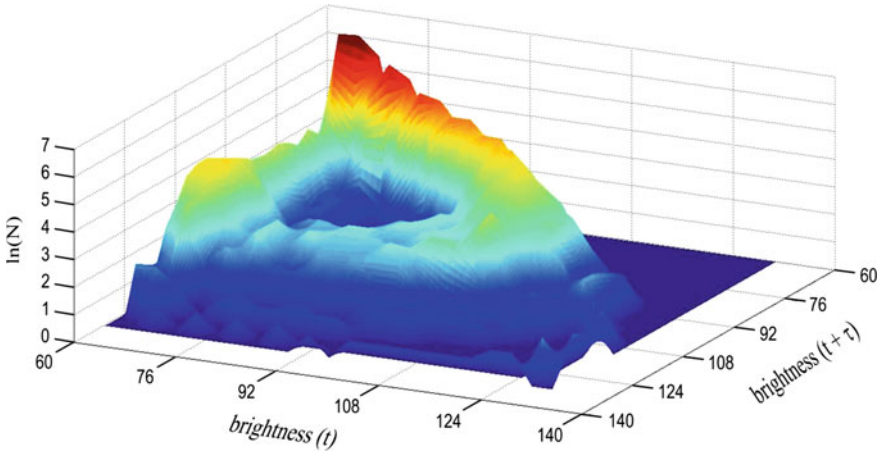

Fig. 6.8 3D Histogram reconstructed from the experimental time series, plotting the trajectory of in the $(B(t), B(t+\tau))$ phase space as a function of the probability of occurrence

cycle turns into a crater-like structure (see Fig. 6.8) on the top and slopes of which the dynamical trajectories propagate.

This example represents a strong sign in favor of the existence of stochastic attractors at the nanoscale, and hence of the validity of the stochastic approaches, generally speaking. Other predictions based on the Fokker-Planck equation can be checked experimentally with the same type of time series. To show this, we here reproduce the derivation of Gaspard [5]. For very long times, the probability distribution of the first return time (the fluctuating period, $r = 1$) is dominated by the diffusion of the phase, so that its variance is given by $\sigma_T^2 = \Omega^{-1} |\partial T/\partial E|$ (see (6.30)). Moreover, the autocorrelation function of a noisy chemical oscillator can be expressed as

$$C(t) \equiv \Omega^2 \langle x_i(t) x_i(0) \rangle \tag{6.31}$$

and it can be shown to take the simple form

$$C(t) \simeq \Omega^2 \sum_{n=-\infty}^{+\infty} |a_n|^2 \mathrm{e}^{s_n t}, \tag{6.32}$$

with the eigenvalues s_n being complex numbers with a negative real part:

$$s_n = -\frac{|\partial T/\partial E|}{2\Omega T} \left(\frac{2\pi n}{T}\right)^2 + i\frac{2\pi n}{t}. \tag{6.33}$$

The above results means that the autocorrelation function is an oscillating function whose amplitude decreases as time goes on. Indeed, it is a combination of Fourier

modes, the amplitude of each of which will eventually relax to zero after a typical time $\simeq |\mathrm{Re}(s_n)|^{-1}$. The relaxation time of the first nontrivial mode $n = \pm 1$

$$\tau \simeq \frac{\Omega\, T^3}{2\pi^2 |\partial T/\partial E|} \tag{6.34}$$

corresponds to the relaxation time of the envelope of the autocorrelation function. It marks a temporal threshold after which the noise takes over the dynamics and the oscillations become uncorrelated: It is therefore called the *correlation time*. We note that the variance of the first return time and the correlation time are not independent, but are instead connected by the universal relation

$$\ln \frac{\tau}{T} \simeq \ln \frac{1}{2\pi^2} - \ln \frac{\sigma_T^2}{T^2}, \tag{6.35}$$

which is independent from the details of the dynamics (the derivatives of the period with respect to the pseudo-energy cancel each other). Analyses performed over different time series for the above reaction showed that this relation is indeed respected for the system under consideration (see Fig. 6.9). This result represents yet another indication that the Fokker-Planck approach is relevant for studying chemical reactions at the nanoscale.

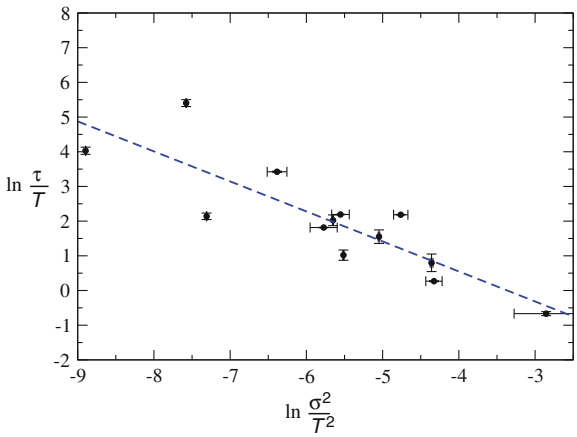

Fig. 6.9 This figure plots the logarithm of the relative correlation time of the autocorrelation function of the signal, as a function of the logarithm of the relative variance of the period of oscillations for the NO_2 + H_2 reaction. The points correspond to periodic behaviors observed at different pressures of the reactants (see [25]). The *dashed line* is the best linear fit of the data. Its intercept ($-(2.9 \pm 0.1)$) and slope ($-(0.9 \pm 0.3)$) are consistent with the proposed scaling, as discussed in the text

6.5 Discussion and Conclusions

The rapid development of nanotechnologies has led to the design of reactive systems with a very small size. Just like their macroscopic counterpart, these nanosystems can be subject to nonlinear, out-of-equilibrium reactive processes. A rigorous and reliable theoretical framework thus needs to be adopted to assess the type of complex phenomena, such as oscillations, chaos or instabilities, that could arise in such circumstances. This step represents a necessary condition for any further development of reactive nanotechnologies.

In this contribution, we showed that the approach based on a stochastic description of reactive events leads to predictions that are qualitatively and quantitatively confirmed by atomic microscopy. In particular, stochastic attractors can be extracted from these experiments, which have the features predicted by the weak-noise limit of the chemical master equation, i.e. by the Fokker-Planck equation.

This validation means that one could expect most of the fluctuation-induced behaviors identified in studies based on the master equation to be found in materials made of reactive nano-objects. The never-ending transitions between multiple steady states is one of these possibilities. Such situations endanger the controllability and the efficiency of these materials. In particular, one should expect fluctuations to affect their yield, their selectivity and their energetic efficiency. A stochastic non-equilibrium thermodynamics will be necessary in order to predict and optimize the behavior of these objects. The construction of such a self-consistent theory is still a work in progress, despite some recent impressive developments including the discovery of different types of fluctuation theorems, which can be seen as stochastic generalizations of the macroscopic laws of thermodynamics [26–29]. Advanced experimental techniques such as those presented here should be used to confirm or invalidate the predictions of the many theoretical frameworks that have been developed so far.

References

1. N.G. van Kampen, *Stochastic Process in Physics and Chemistry*, 3rd edn. (Elsevier North Holland Personal Library, North-Holland, 2007)
2. D. Gillespie, J. Chem. Phys. **113**, 297 (2000)
3. R. Kubo, K. Matsuo, K. Kitahara, J. Stat. Phys. **9**, 51 (1973)
4. W. Vance, J. Ross, J. Chem. Phys. **105**, 479 (1996)
5. P. Gaspard, J. Chem. Phys. **117**, 8905 (2002)
6. M.I. Freidlin, A.D. Wentzell, in *Random Perturbations of Dynamical Systems* (Springer-Verlag, Berlin, 1984)
7. R. Graham, D. Roekaerts, T. Tel, Phys. Rev. A **31**, 3364 (1985)
8. E.W. Müller, Z. Naturforsch. **11**a, 88 (1956)
9. A.J. Melmed, Appl. Surf. Sci. **94/95**, 17 (1996)
10. M.K. Miller, A. Cerezo, M.G. Hetherington, G.D.W. Smith, in *Atom Probe Field Ion Microscopy* (Clarendon Press, Oxford, 1996)
11. T. Visart de Bocarmé, G. Beketov, N. Kruse, Surf. Interface Anal. **36**, 522 (2004)

12. N. Kruse, T. Visart de Bocarmé, in *Handbook of Heterogeneous Catalysis*, 2nd edn. ed. by G. Ertl, H. Knözinger, F. Schüth, J. Weitkamp (Wiley-VCH Verlag GmbH and Co. KGaA, Weinheim, Germany, 2008)
13. J.-S. McEwen, P. Gaspard, T. Visart de Bocarmé, N. Kruse, Proc. Natl. Acad. Sci. USA **106**, 3006 (2009)
14. J.-S. McEwen, P. Gaspard, T. Visart de Bocarmé, N. Kruse, J. Phys. Chem. C **113**, 17045 (2009)
15. T. Visart de Bocarmé, T. Bär, N. Kruse, Ultramicroscopy **89**, 75 (2001)
16. Y. De Decker, H. Marbach, M. Hinz, S. Günther, M. Kiskinova, A.S. Mikhailov, R. Imbihl, Phys. Rev. Lett. **92**, 198305 (2004)
17. D.T. Gillespie, J. Phys. Chem. **81**, 2340 (1977)
18. Yu. Suchorski, J. Beben, E.W. James, J.W. Evans, R. Imbihl, Phys. Rev. Lett. **82**, 1907 (1999)
19. D.H. Parker, M.E. Bartram, B.E. Koel, Surf. Sci. **217**, 489 (1989)
20. C. Barroo, Y. De Decker, T. Visart de Bocarmé, N. Kruse, J. Phys. Chem. C **118**, 6839 (2014)
21. C. Barroo, S.V. Lambeets, F. Devred, T.D. Chau, N. Kruse, Y. De Decker, T. Visart de Bocarmé, New J. Chem. **38**, 2090 (2014)
22. V. Gorodetskii, J.H. Block, W. Draschel, Appl. Surf. Sci. **76/77**, 129 (1994)
23. F. Takens, in *Symposium on Dynamical Systems and Turbulence*, ed. by D.A. Rand, L.-S. Young (Springer, Berlin, 1981), p. 366
24. T. Sauer, J.A. Yorke, M. Casdagli, J. Stat. Phys. **65**, 579 (1991)
25. C. Barroo, Y. De Decker, T. Visart de Bocarmé, P. Gaspard, J. Phys. Chem. Lett. **6**, 2189 (2015)
26. R.J. Harris, G.M. Schütz, J. Stat. Mech. P07020 (2007)
27. M. Esposito, C. Van den Broeck, Phys. Rev. E **82**, 011143 and 011144 (2010)
28. U. Seifert, Rep. Prog. Phys. **75**, 126001 (2012)
29. Y. De Decker, Physica A **428**, 178 (2015)